Molecularly imprinted polymer nanoparticles-based electrochemical chemosensors for selective determination of cilostazol and its pharmacologically active primary metabolite in human plasma

Jyoti Yadav, Carlo Gonzato, Teresa Żolek, Dorota Maciejewska, Andrzej Kutner, Franck Merlier, Karsten Haupt, Piyush Sindhu Sharma, Krzysztof Noworyta, Wlodzimierz Kutner

Version of Record: https://www.sciencedirect.com/science/article/pii/S0956566321005790
Manuscript_99f623a3ad8f3b33e8364b035a4ec800

Revised

Molecularly imprinted polymer nanoparticles-based electrochemical chemosensors for selective determination of cilostazol and its pharmacologically active primary metabolite in human plasma

Jyoti,[1] *Carlo Gonzato,*[2] *Teresa Żołek,*[3] *Dorota Maciejewska,*[3] *Andrzej Kutner,*[4] *Franck Merlier,*[2] *Karsten Haupt,*[2,*] *Piyush Sindhu Sharma,*[1] *Krzysztof R. Noworyta,*[1,**] *and Wlodzimierz Kutner*[1, 5,**]

[1] Institute of Physical Chemistry, Polish Academy of Sciences (IPC PAS), Kasprzaka 44/52, 01-224 Warsaw, Poland

[2] Université de Technologie de Compiègne, CNRS Laboratory for Enzyme and Cell Engineering UMR 7025, Rue du Docteur Schweitzer, 60203, Compiègne, France

[3] Department of Organic Chemistry, Faculty of Pharmacy, Medical University of Warsaw, Banacha 1, 02-097 Warsaw, Poland

[4] Department of Bioanalysis and Drug Analysis, Faculty of Pharmacy, Medical University of Warsaw, Banacha 1, 02-097 Warsaw, Poland

[5] Faculty of Mathematics and Natural Sciences. School of Sciences, Cardinal Stefan Wyszynski University in Warsaw, Woycickiego 1/3, 01-815 Warsaw, Poland

---

* Corresponding author from Université de Technologie de Compiègne.

** Corresponding authors from Institute of Physical Chemistry, Polish Academy of Sciences.

E-mail addresses: karsten.haupt@utc.fr (K. Haupt), knoworyta@ichf.edu.pl (K. Noworyta), wkutner@ichf.edu.pl (W. Kutner).

Abstract

Molecularly imprinted polymer (MIP) nanoparticles-based differential pulse voltammetry (DPV) and electrochemical impedance spectroscopy (EIS) chemosensors for antiplatelet drug substance, cilostazol (**CIL**), and its pharmacologically active primary metabolite, 3,4-dehydrocilostazol (**dhCIL**), selective determination in human plasma were devised, prepared, and tested. Molecular mechanics (MM), molecular dynamics (MD), and density functional theory (DFT) simulations provided the optimum structure and predicted the stability of the pre-polymerization complex of the cilostazol template with the chosen functional acrylic monomers. Moreover, they accounted for the MIP selectivity manifested by the molecularly imprinted cavity with the cilostazol molecule complex stability higher than that for each interference. On this basis, a fast and reliable method for determining both compounds was developed to meet an essential requirement concerning the personalized drug dosage adjustment. The limit of detection (LOD) at the signal-to-noise ratio of $S/N = 3$ in DPV and EIS determinations using the ferrocene redox probe in a "gate effect" mode was 93.5 (±2.2) and 86.5 (±4.6) nM **CIL**, respectively, and the linear dynamic concentration range extended from 134 nM to 2.58 μM in both techniques. The chemosensor was highly selective to common biological interferences, including cholesterol and glucose, and less selective to structurally similar dehydroaripiprazole. Advantageously, it responded to 3,4-dehydrocilostazol, thus allowing for the determination of cilostazol and 3,4-dehydrocilostazol together. The EIS chemosensor appeared slightly superior to the DPV chemosensor concerning its selectivity to interferences. The cilostazol DPV sorption data were fitted with Langmuir, Freundlich, and Langmuir-Freundlich isotherms. The determined sorption parameters indicated that the imprinted cavities were relatively homogeneous and efficiently interacted with the **CIL** molecule.

Keywords

Molecularly imprinted polymer nanoparticle, nanoMIP; Electrochemical chemosensor; Cilostazol; 3,4-Dehydrocilosazol; Drug dosage control; Sorption modeling with molecular dynamics, MD, and density functional theory, DFT

1. Introduction

Cilostazol, 6-[4-(1-cyclohexyl-1H-tetrazol-5-yl)butoxy]-3,4-dihydro-2(1H)-quinolinone, **CIL**, (Figure 1a) is an oral selective cyclic nucleotide phosphodiesterase 3 (PDE_3) inhibitor with antiplatelet, vasodilatory, and antimitogenic effects (Ikeda et al., 2013; Saitoh et al., 1993). This inhibitor increases cAMP that, in turn, increases protein kinase A in its active form, directly related to inhibition in platelet aggregation. It is used to treat intermittent claudication (IC), a symptom of peripheral arterial disease (PAD) (Bramer et al., 1999; Douglas et al., 2005), most commonly caused by atherosclerosis. It affects millions of patients worldwide, causing significant morbidity and mortality (Zhao et al., 2010).

Moreover, **CIL** is helpful for the treatment of diabetic (Bramer et al., 1999; Douglas et al., 2005; Lee et al., 2008; Zhao et al., 2010), and Alzheimer's patients (Hiramatsu et al., 2010; Hishikawa et al., 2017; Park et al., 2011; Saito and Ihara, 2014; Sakurai et al., 2013). Several small-scale clinical trials were conducted for evaluating the efficacy of **CIL** in patients with mild cognitive impairment (MCI) (Taguchi et al., 2013), Alzheimer's disease (AD), and cardiovascular disease (CVD) (Hishikawa et al., 2017; Park et al., 2011; Sakurai et al., 2013). In addition, new therapeutic applications of **CIL** alone or in combination with other drug substances are under extensive clinical development (NIH U.S. National Library of Medicine, ClinicalTrials.gov, 2021). For examining these effects on a larger scale, randomized placebo-controlled phase II trials are ongoing on patients with MCI and Alzheimer's disease (Saito and Ihara, 2014). Therefore, a fast and reliable method for the non-invasive **CIL** determination in large sets of clinical samples is highly demanded. Independent studies revealed that after (50 to 200)-mg dose oral administration of **CIL**, its concentration in plasma increased to 806 (±238) µg/L after 3 h, and then decreased to ≥ 20 µg/L while in the urine samples, the 3,4-dehydrocilostazol (**dhCIL)** metabolite predominated. Apparently, metabolic rather than urinary excretion is the primary elimination route for **CIL** (Bramer et al., 1999).

CYP3A4 and CYP2C19, two isoenzymes of the cytochrome P450 system, metabolize **CIL** to ~11 different metabolites with **dhCIL** (Figure 1a) being the primary pharmacologically active metabolite (Akiyama et al., 1985). For **CIL** determination in biological matrices, several analytical procedures were developed, including simultaneous determination of **CIL** and **dhCIL**, along with anti-inflammatory drugs (Akiyama et al., 1985; Bhatt et al., 2015; Bramer et al., 2001; Nirogi et al., 2006). Nowadays, **CIL** is

determined in human plasma using methods mostly involving electrospray ionization tandem mass spectrometry (ESI/MS/MS) (Bramer et al., 2001), high-performance liquid chromatography (HPLC) (Pareek et al., 2014; Yeon et al., 2005), (liquid chromatography)-(electrospray ionization tandem mass spectrometry) (HPLC-ESI/MS/MS) (Nirogi et al., 2006), or spectrofluorometry (Ibrahim et al., 2016). Unfortunately, all these methods are laborious, time-consuming, and require expensive instrumentation. Moreover, they all need highly skilled operators to perform reliable determinations. Therefore, there is a need for an inexpensive, sensitive, and easy-to-operate sensor for selective **CIL** and **dhCIL** determination.

a

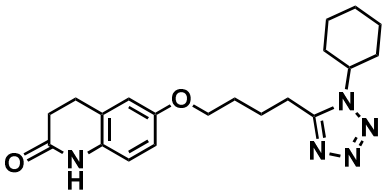

1

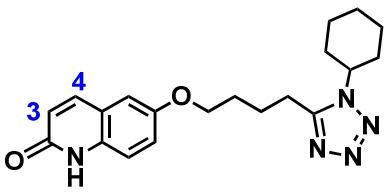

2

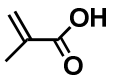

3

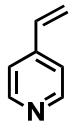

4

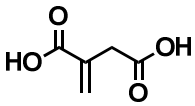

5

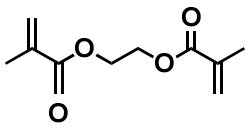

6

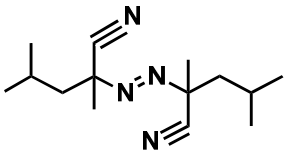

7

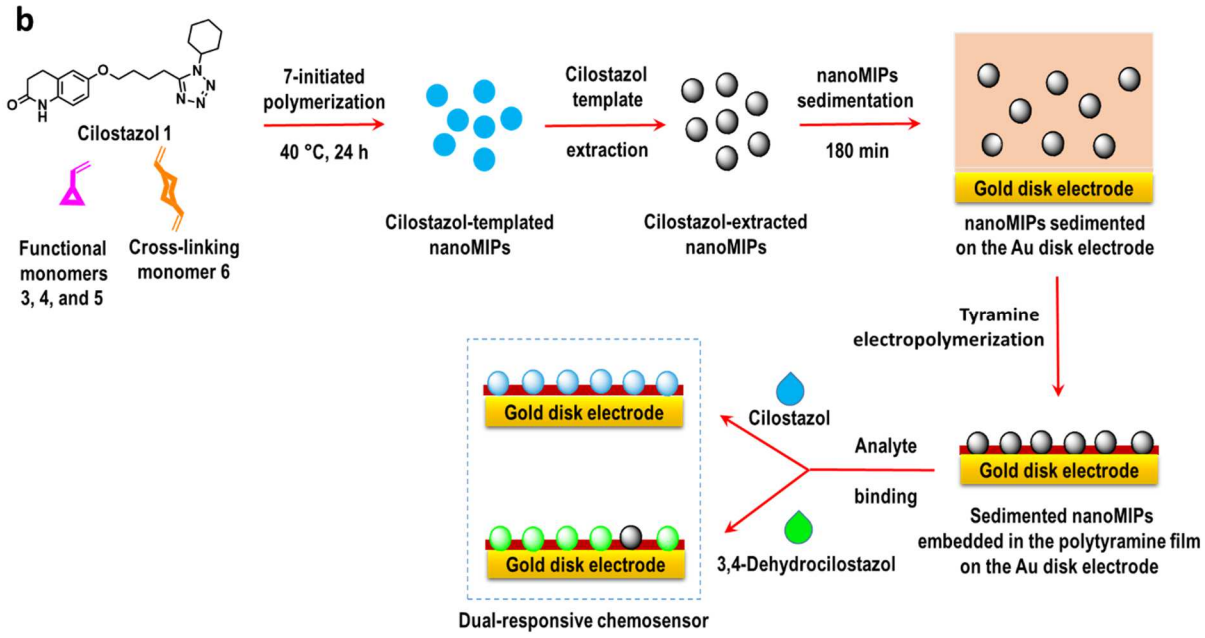

Figure 1. (a) Structural formulas of the cilostazol (**CIL**, **1**) and it's primary pharmacologically active metabolite 3,4-dehydrocilostazol (**dhCIL**, **2**) analytes, the methacrylic acid (**MAA**, **3**), 4-vinylpyridine (**4-VP**, **4**), and itaconic acid (**IA**, **5**) functional monomers, as well as the ethylene glycol dimethylacrylate (**EGDMA**, **6**) cross-linking monomer and the 2,2'-azobis(2,4-dimethylvaleronitrile) (**ABDV**, **7**) initiator. (b) Flowchart of electrochemical chemosensor preparation.

For that purpose, herein, molecularly imprinted polymer (MIP) nanoparticles (nanoMIPs) were prepared (Figure 1b). MIPs are artificial receptors made by imprinting template molecules in a polymer matrix. Then, those are removed via, e.g., solvent extraction, thus vacating imprinted molecular cavities. These cavities' size, shape, and orientation of their recognizing sites complement the size, shape, and orientation of binding sites of the template molecule (Belbruno, 2019; Haupt and Mosbach, 2000). Therefore, an MIP is expected to bind template molecules stronger than other, even structurally similar molecules.

Molecular imprinting in polymers is versatile (Ramanavicius et al., 2021; Ramanavicius and Ramanavicius, 2021). It opens doors to many applications, including purification and separation (Azizi and Bottaro, 2020; Ndunda and Mizaikoff, 2016; Rutkowska et al., 2018), drug delivery (Ahmad et al., 2019; Puoci et al., 2011), chemosensing (Haupt and Mosbach, 2000; Sharma et al., 2018), catalysis (Wulff et al., 2002), and analyte determination (Bedwell and Whitcombe, 2016; Goud et al., 2021; Xie et al., 2016) to name just a few. The latter has already been employed for determining a broad assortment of target analytes ranging from small-molecule compounds (e.g., amino acids and sugars) to macromolecular compounds (e.g., peptides, proteins, and nucleic acids) as well as cells and even whole microorganisms

(Ahmad et al., 2019; Haupt et al., 2020; Yang et al., 2005). Several reports claim MIPs as alternatives to antibodies (Haupt et al., 2020; Vlatakis et al., 1993; Yarman et al., 2021). The most impressive advantage of MIPs is their physical and chemical resistance, straightforward preparation, and easy coupling to different substrates or integration with different device transducers.

MIPs prepared via traditional bulk polymerization are heterogeneous, and their recognizing ability is relatively low (Dong et al., 2021; El-Schich et al., 2020). For overcoming this limitation, nanoMIPs were devised (Haupt et al., 2020; Poma et al., 2013). NanoMIPs have attained much attraction because of their high (surface area)-to-volume ratio, providing high accessibility to target species and significantly increasing the binding ability and kinetics. However, this ability relies on the precise selection of the parameters that influence the imprinting. Several vital issues, including the selection of functional (FM) (Cummins et al., 2006; Yilmaz et al., 1999), and cross-linking (CL) monomers (Karlsson et al., 2004), a porogenic solvent (Pérez-Moral and Mayes, 2004), initiators (Mijangos et al., 2006), polymerization procedures (Vaughan et al., 2007), polymerization time (O'Shannessy et al., 1989), and polymerization temperature (O'Shannessy et al., 1989) influence the imprinting.

By precipitation polymerization, we have herein synthesized **CIL**-templated nanoMIPs (Figure 1b). This polymerization is relatively facile, resulting in evenly dispersed micro- and nano-beads without any additives, including stabilizers (Chaitidou et al., 2008; Ye et al., 1999). Generally, this procedure uses a solvent, where the monomers, the initiator, and the template are dissolved, but the resulting polymer is not, thus forming a precipitate of micro- or nanoMIPs. After removal of **CIL**, binding tests allowed us establishing the efficiency of these nanoMIPs and their selectivity.

The performed molecular mechanics (MM), molecular dynamics (MD), and density functional theory (DFT) simulations confirmed the stoichiometry and stability of both the pre-polymerization complex of **CIL** with the functional and cross-linking monomers chosen as well as **CIL** and each interference, separately, with the molecular cavity, imprinted with **CIL** in nanoMIPs, towards nanoMIP selectivity.

NanoMIPs with the highest **CIL** binding efficiency were then chosen to fabricate chemosensors to determine **CIL** and **dhCIL**. For that, the nanoMIPs were embedded in a polytyramine film, deposited by electropolymerization on Au disk electrodes (Figure 1b). The nanoMIPs molecular cavities' binding **CIL** and **dhCIL** abilities were evaluated using the "gate effect" (Sharma et al., 2019; Yoshimi et al., 2001). Moreover, **CIL** was determined in

human plasma. Because few earlier reported electrochemical chemosensors for **CIL** lack interferences studies confirming the chemosensor suitability for practical use (Attia et al., 2011; Jain and Sharma, 2012), we strongly believe that our present research provides unique detailed results on the electrochemical chemosensing in the human plasma of **CIL** and **dhCIL**, in which the matrix effect is considered.

2. Experimental

2.1 Materials and procedures

2.1.1 Materials

Cilostazol (**CIL**) was synthesized in the Chemistry Department of the Łukasiewicz Research Network - Pharmaceutical Research Institute, whereas methacrylic acid (**MAA**, 99%, CAS No. 79-41-4), 4-vinylpyridine (**4-VP**, CAS No. 100-43-6), itaconic acid (**IA**, ≥ 99 %, CAS No. 97-65-4), ethylene glycol dimethylacrylate (**EGDMA**, CAS No. 97-90-5), **cholesterol**, β-D(+) **glucose** (97%, CAS no. 492-61-5), anhydrous acetonitrile (HPLC grade), octanenitrile, glacial acetic acid, and ferrocene (98%, CAS No. 102-54-5) were purchased from Sigma-Aldrich. 2,2'-Azobis(2,4-dimethylvaleronitrile), (**ABDV**, CAS No. 4419-11-8) was from DuPont Chemicals. All reagents and solvents were of analytical grade, unless stated otherwise, and used as received except for **4-VP**, distilled under decreased pressure before use. The tetrabutylammonium perchlorate (TBA)ClO_4 (≥ 99%, CAS No. 1923-70-2), a supporting electrolyte of the electrochemical grade, was purchased from Sigma-Aldrich. Reference standards for bioanalysis, 3,4-dehydrocilostazol (**dhCIL**, CAS No. 73963-62-9) and dehydroaripiprazole-d8 (CAS No. 129722-25-4), were purchased from Toronto Research Chemicals, Canada. Deionized (18.2 MΩ cm) Milli-Q® water (EMD Millipore, Billerica, MA, US) was used for the preparation of solutions.

2.1.2 nanoMIPs synthesizing via precipitation polymerization

For nanoMIPs preparation (Figure 1b, Table 1), a mixture of **CIL** (0.2 mmol), **MAA** (1.6 mmol), **EGDMA** (5 mmol), and **ABDV** (0.04 mmol) was dissolved in acetonitrile (15 mL) in a glass vial sealed with a silicone septum (Figure 1a). The (functional monomer)-to-template molar ratio used was 8 : 1 to drive the self-assembly complexation equilibrium toward forming a pre-polymerization complex. The resulting solution of the complex was deoxygenated with a nitrogen purge for 15 min on ice. The polymerization was allowed to proceed overnight at 40 °C and then ceased by exposure to air. Subsequently, precipitated

nanoMIPs were collected by centrifugation, then triply rinsed, under agitation, at 60 °C with the methanol : (acetic acid) (9 : 1, *v/v*) solution, followed by double rinsing with the ethanol : (acetic acid) (9 : 1, *v/v*) solution, afterward double rinsing with ethanol, and then one rinsing with methanol. Finally, the nanoMIPs were dried overnight (16 h) under decreased pressure (3 mbar) at room temperature (~25 °C).

Control, non-imprinted polymer nanoparticles, nanoNIPs, were synthesized the same way, except for the absence of **CIL**.

Moreover, three other nanoMIPs and their corresponding nanoNIPs were prepared (Section S2 in Supplementary data) using **4-VP** and **IA** functional monomers in either acetonitrile or octanenitrile solvent (15 mL).

2.1.3 nanoMIPs and nanoNIPs immobilizing in polytyramine films on electrodes

NanoMIPs or nanoNIPs (0.250 mg each) were suspended in 10 mM tyramine in 25 mM H_2SO_4 (0.250 mL). The resulting suspension was ultrasonicated for 5 min. For these NPs sedimentation, a 2-mm diameter Au disk electrode was fixed upside down, then a 1-mL pipette tip with a cut-off end was mounted on its top. Next, this tip was filled with the suspension to allow NPs sedimentation for 3 h (Figure S16 in Supplementary data). On the surface of this electrode, subsequently, a polytyramine (Figure S5c in Supplementary data) film was potentiodynamically deposited using 15 potential cycles between 0 to 1.50 V vs. Ag quasi-reference electrode at a potential scan rate of 50 mV s^{-1} for the NPs embedding in this film (El-Akaad et al., 2020). Afterward, the electrode was rinsed with 25 mM H_2SO_4 then acetonitrile to remove residual unreacted monomers.

2.1.4 Other procedures

Details of electrochemical measuring, nanoMIPs binding of **CIL**, AFM and SEM imaging, determining of **CIL** by HPLC, size of nanoMIPs and nanoNIPs estimating by DLS, depositing polytyramine films by potentiodynamic electropolymerization, preparing a **CIL**-spiked plasma solution, **CIL**-induced protein precipitating in human plasma, investigating chemosensors selectivity to interferences and their performance in human plasma, and computer simulations' procedures are described in Sections S3 and S4 in Supplementary data.

2.2 Instrumentation

Instruments applied in all experiments are described in Section S1 in Supplementary data.

3. Results and discussion

3.1 Optimizing nanoMIPs composition

For optimizing the nanoMIPs composition, we synthesized nanoMIPs at different FM and CL combinations and ratios with assessing their affinity for **CIL** by HPLC (Figures S1 and S2 in Supplementary data). Aiming at small, globular particles to interface with an electrode, we found nanoMIP synthesis by precipitation polymerization in acetonitrile as a promising possibility. This porogenic solvent is often used to synthesize imprinted sub-micrometer-sized particles (Alexander et al., 2006), predominantly via noncovalent imprinting based on hydrogen bonding. Thus, the presence of the lactam group on a **CIL** molecule is suitable for H-binding. High **CIL** solubility in acetonitrile prompted us to test some FMs, commonly used together with this solvent, to imprint molecular cavities in nanoMIPs by incurring H-bonding. The tested FMs included **MAA**, **4-VP**, and **IA** (Table 1). Among them, **MAA** is, perhaps, the most widely used for the synthesis of nanoMIPs. Moreover, **IA** is a common (carboxylic acid)-based FM, which can afford multiple interactions thanks to its dual functionality. Besides, **4-VP** is used to raise π-π stacking in aqueous solutions (e.g., Haupt et al., 1998,) but, in acetonitrile, it can also build a synergistic effect with **MAA** (e.g., Fuchs et al., 2011). Furthermore, the presence of aromatic moieties, such as a tetrazole and a 6-membered ring close to the lactam moiety on a **CIL** molecule suggests that the application of **4-VP** might be promising.

The nanoMIPs, prepared solely using functional monomer **MAA**, bound **CIL** stronger than other synthesized nanoMIPs did (Figure S2a in Supplementary data). Surprisingly, the exchange of **IA** for **MAA** to serve as the FM did not improve the nanoMIPs properties. Instead, it somewhat increased the non-specific binding on nanoNIPs despite twice as many available carboxyl groups on the **MAA** molecule. Further, replacing acetonitrile with octanenitrile, a lower-polarity solvent favoring H-binding, appeared unsuccessful in improving the nanoMIP-C binding capacity (Figure S2c).

Next, for each monomer combination used to prepare nanoMIPs, the binding capacity of the nanoMIPs to **CIL** was determined (Table 1). Apparently, this capacity is the highest for nanoMIP-A. Therefore, this polymer was further used for chemosensor preparation. For different nanoMIPs, the order of the determined binding capacity was the same as that of the

calculated Gibbs free energy changes ($\Delta G_{complex}$), i.e., predicted stability, of the pre-polymerization complexes formed in solution (Table 1, Figure 2 and Figure S3 in Supplementary data).

Table 1. Composition of different cilostazol-templated nanoMIPs, NPs preparation conditions, the binding capacity determined, and the Gibbs free energy change due to the formation of a pre-polymerization complex in a solution using the ethylene glycol dimethylacrylate (**EGDMA**) cross-linking monomer and the 2,2'-azobis(2,4-dimethylvaleronitrile) (**ABDV**) initiator, at 40 °C ($\Delta G_{complex}$), as well as the complex of the imprinted cavity with the **CIL** molecule (ΔG_{bind}).

Polymer	Functional monomer FM1	Functional monomer FM2	Molar ratio of **CIL** : FM1 : FM2	Solvent	Normalized binding capacity for 15 mg nanoMIPs/ mL	$\Delta G_{complex}$ (kJ/mol)	$\Delta G_{bind}{}^{e}$ (kJ/mol)
nanoMIP-A	**MAA**	-	1 : 8 : 0	Acetonitrile	24.8	-323.79[a]	-192.20
nanoMIP-B	**MAA**	**4-VP**	1 : 4 : 4	Acetonitrile	5.8	-256.12[b]	-175.17
nanoMIP-C	**MAA**	**4-VP**	1 : 4 : 4	Octanenitrile	0.4	-46.45[b]	-75.99
nanoMIP-D	**IA**	-	1 : 8 : 0	Acetonitrile	4.48	-128.14[a]	-94.46

[a] $\Delta G_{complex} = \Delta G_{system} - \Delta G_{cilostazol} - 8\Delta G_{FM1} - 25\Delta G_{CL}$

[b] $\Delta G_{complex} = \Delta G_{system} - \Delta G_{cilostazol} - 4\Delta G_{FM1} - 4\Delta G_{FM2} - 25\Delta G_{CL}$

$\Delta G_{complex}$, ΔG_{system}, $\Delta G_{cilostazol}$, ΔG_{FM1}, ΔG_{FM2}, and ΔG_{CL} stand for the Gibbs free energy change originating from the formation of a pre-polymerization complex, the whole system, cilostazol, FM1, FM2, and CL in acetonitrile or octanenitrile, respectively.

[e] Values of $\Delta G_{bind}{}^{e}$ were calculated using equation S1 in Supplementary data.

Because of a normalized binding capacity to **CIL** relatively high, nanoMIP-B might be another candidate for chemosensor preparation. However, **CIL** template complete removal from the nanoMIP-B appeared difficult. Over 50 extraction rounds were needed for that. Therefore, nanoMIP-B was not used any further.

Moreover, the nanoMIP cavities structures were simulated (Figure 2 and Figure S3 in Supplementary data), and the stability of their complexes with **CIL** was calculated (Table 1) to rationalize the selection of the monomers. As expected, the Gibbs free energy changes due to cavity interactions with **CIL** (ΔG_{bind}) followed those of the experimental binding capacity of the nanoMIPs to **CIL** (Table 1), thus confirming the experimental results.

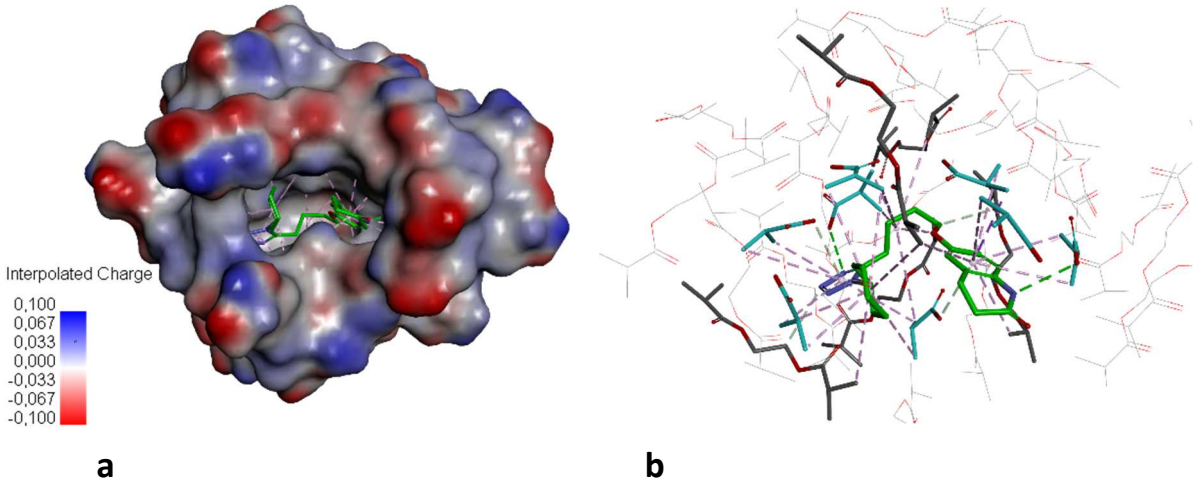

Figure 2. Simulated structures of the (a) space-filling and (b) skeleton models of the nanoMIP-A cavity (**CIL** : **MAA** : **EGDMA** = 1 : 8 : 25 in the acetonitrile porogen) with the **CIL** molecule embedded. In the space-filling model, the surface distribution of the molecular electrostatic potential (MEP) is colored according to the interpolated (blue) positive and (red) negative charge. In the skeleton model, the primary interactions responsible for selectivity are classical hydrogen bonds indicated with green dash lines, non-classical hydrogen bonds with grey dash lines, and hydrophobic interactions with pink dash lines.

3.2 Microscopic imagining of nanoMIPs immobilized in the polytyramine films on electrodes

Optimizing the electrode surface coverage with nanoMIPs embedded in the polytyramine film is crucial for superior chemosensor performance. Accordingly, complete coverage of nanoMIPs can block the diffusion of analyte molecules to nanoMIP molecular cavities. Furthermore, an insufficient thickness of the film can affect the mechanical stability of the polymer NP layer on the other. The AFM determined average surface roughness and thickness of the film were 27 (±4) and 170 (±30) nm. The latter value is close to the DLS determined average solvodynamic nanoMIPs and nanoNIPs size of 160 (±20) and 157 (±19) nm, respectively (Section S6 and Figure S4 in Supplementary data). Apparently, the (polytyramine film)-embedded nanoparticles were partially exposed. The SEM (Figure 3) and AFM (Section S5 and Figure S6 in Supplementary data) imaging confirmed the presence of the incompletely encapsulated nanoMIPs in this film.

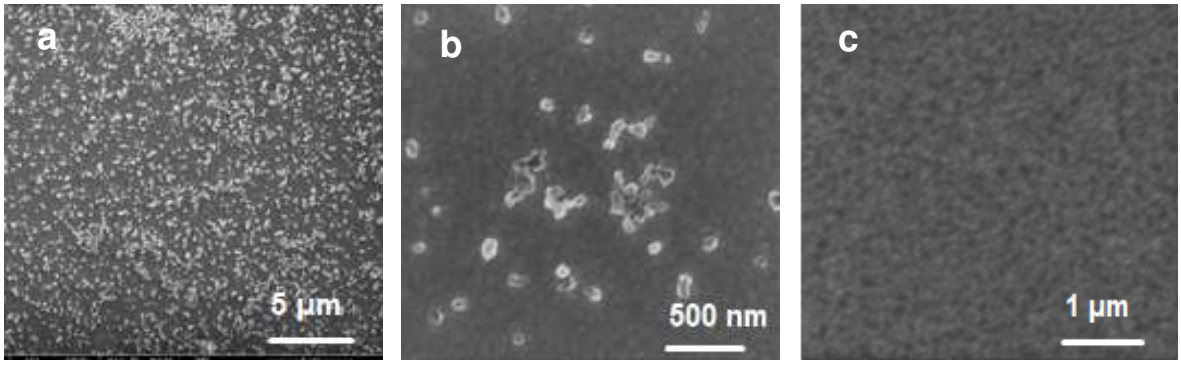

Figure 3. SEM images of (a) and (b) the nanoMIPs embedded in the polytyramine film. (c) a plain polytyramine film deposited on the Au-layered glass slide electrode.

3.3 Electrochemical characterizing nanoMIPs immobilized in polytyramine films on electrodes

Choosing the most appropriate nanoMIPs immobilization procedure is vital for effectively integrating them with a transducer surface, here on the electrode surface, to prepare an MIP chemosensor. Polymer film deposition by electropolymerization is an attractive alternative to chemical polymerization for the robust integration of an MIP recognition element with a conducting transducer (Chen et al., 2016; Zhao et al., 2018). Furthermore, compared to other immobilization procedures, the MIP attachment by electropolymerization has an intrinsic ability to control the film's morphology by adjusting the appropriate deposition conditions, including the deposition time and the potential applied. Therefore, it is used in a broad range of applications for integrating functional nanomaterials into the deposited films. (Ezoji and Rahimnejad, 2019; Tonelli et al., 2019). Herein, we immobilized polymer NPs in a polytyramine film by multi-cyclic potentiodynamic deposition (Section S7 and Figure S5b in Supplementary data). There is one anodic and one cathodic peak at 0.80 and 0.46 V vs. Ag quasi-reference electrode, respectively, in the potentiodynamic curve recorded. The anodic peak decreased in the initial few cycles, then increased, and, later, it became constant. This behavior was similar to that of polytyramine potentiodynamic deposition in the absence of NPs (Figure S5a in Supplementary data), indicating polytyramine film deposition. However, there was no direct evidence of nanoMIPs immobilization in the polytyramine film. Figure S5c in Supplementary data shows the estimated structural formula of polytyramine.

Both the cyclic voltammetry (CV) (curve *3* in Figure S7a in Supplementary data) and differential pulse voltammetry (DPV) (curve *3′* in Figure S7b in Supplementary data) peak currents in the ferrocene solution of acetonitrile at the electrode coated with the

polytyramine/ nanoMIPs film, were suppressed. Moreover, the polytyramine film alone blocked electro-oxidation of ferrocene (curves *2* and *2′* in Figure S7a and S7b, respectively, in Supplementary data). However, the diameter of the semicircle in the electrochemical impedance spectroscopy (EIS) Nyquist plot for the polytyramine/nanoMIPs, ~91 kΩ, was much larger (curve *3″* in Figure S7c in Supplementary data) than that for the polytyramine film alone, 8.4 kΩ (curve *2″* in Figure S7c in Supplementary data). Thus, the polytyramine/nanoMIPs film blocked the electrode more extensively (Section S8 in Supplementary data).

3.4 Optimizing conditions of polymer NPs immobilization on electrodes

The nanoMIPs were allowed to sediment for four different time intervals, vis., 30, 150, 180 min, and 24 h (Section S9 and Figure S8a in Supplementary data), followed by potentiodynamic polytyramine film deposition. For the firm holding of the polymer NPs, this electropolymerization was optimized using different tyramine concentrations.

If nanoMIPs were sedimented for merely 30 min, the resulting chemosensor detectability of **CIL** (curve *2* in Figure S8a in Supplementary data) was similar to that obtained using a genuine polytyramine film (curve *1* in Figure S8a in Supplementary data). Evidently, an insufficient amount of nanoMIPs was immobilized during 30-min sedimentation. For 150-min (curve *3* in Figure S8a in Supplementary data) and 180-min (curve *4* in Figure S8a, Supplementary data) sedimentation, the normalized DPV peak currents were almost the same, substantiating the full settlement of the NPs. However, 24-h sedimentation deteriorated the chemosensor performance (curve *5* in Figure S8a in Supplementary data). Therefore, 180-min sedimentation was used as optimized for subsequent experiments. If polytyramine was deposited from a solution of higher tyramine concentration, the chemosensor lost its selectivity. That is, the detectability of the **CIL** analyte and dehydroaripiprazole interference was similar (curves *1′* and *2′*, respectively, in Figure S8b in Supplementary data). Presumably, that was because of the extensive coverage of NPs with the polytyramine film. The film deposited in this case is thicker, and diffusion of both the analyte and the redox probe through the film is largely hindered, leading to a weak chemosensor response.

3.5 ***CIL*** *electrochemical determining with the polytyramine-(nanoMIP-A) and polytyramine-(nanoNIPs) film-coated electrodes*

When **CIL** was added to the acetonitrile solution of ferrocene, complementary cavities of the polytyramine-(nanoMIP-A) film, deposited on the electrode, bound **CIL** molecules. Being governed by the gate effect (Yoshimi et al., 2001), this binding resulted in decreasing DPV peak current of ferrocene with an increasing concentration of **CIL** (curves *1 – 8* in Figure 4a). It reached saturation at the **CIL** concentration exceeding 2.5 µM. The normalized DPV peak current $(I_{DPV,0} - I_{DPV,s})/I_{DPV,0})$, where $I_{DPV,0}$ and $I_{DPV,s}$ stand for the initial and actual DPV peak current, was linearly dependent on the logarithm of **CIL** concentration. The linear dynamic concentration range extended from 135 nM to 2.58 µM **CIL** with the calibration plot obeying a semilogarithmic linear regression equation of $(I_{DPV,0} - I_{DPV,s})/I_{DPV,0}) = 0.36\ (\pm 0.01)/\log\ [\mu M] \times \log\ \{c_{cilostazol}\ [\mu M]\} + 0.450\ (\pm 0.006)$ (curve *1″* in Figure 4c). The sensitivity and correlation coefficient were 0.36 (±0.01)/log [µM], and $R^2 = 0.98$, respectively. At the signal-to-noise ratio of $S/N = 3$, the lower limit of detection was LOD = 93.5(±2.2) nM **CIL**.

For the solutions of the same composition, EIS spectra were recorded (Figure 4d) and the normalized ferrocene charge transfer resistance, $(R_{ct,0} - R_{ct,s})/R_{ct,0}$ where $R_{ct,0}$ and $R_{ct,s}$ denotes the initial and actual charge transfer resistance, was determined. The following linear regression equation describes this resistance dependence on the **CIL** concentration. $(R_{ct,0} - R_{ct,s})/R_{ct,0} = -1.07\ (\pm 0.10)\ [1/\mu M] \times c_{cilostazol}\ [\mu M] - 0.09\ (\pm 0.15)$. The sensitivity and the regression coefficient were -1.07 (±0.10) [1/µM] and $R^2 = 0.94$, respectively. At $S/N = 3$, the LOD was 86.5(±4.6) nM **CIL**.

Under the same solution conditions, the DPV peak current changes (Figure 4b and curve *6″* in Figure 4c) and the charge transfer resistance changes (Figure 4e and curve 6^V in Figure 4f) for the nanoNIPs immobilized in the polytyramine film were much smaller than those for the nanoMIPs yielding smaller apparent sensitivity of 0.27 (±0.004) 1/log [µM] and -0.07 (±0.02) [1/µM], respectively. These results indirectly confirm the presence in nanoMIPs of imprinted cavities that enhance **CIL** binding. Furthermore, the apparent imprinting factor, estimated from the ratio of the slopes of **CIL** calibration plots for the nanoMIPs and nanoNIPs film-coated electrodes, was for DPV surprisingly low (IF = 1.34) and for EIS appreciably high (IF = 15.28). This discrepancy in the determined apparent IF values might arise from different effects contributing to the signal measured in each technique.

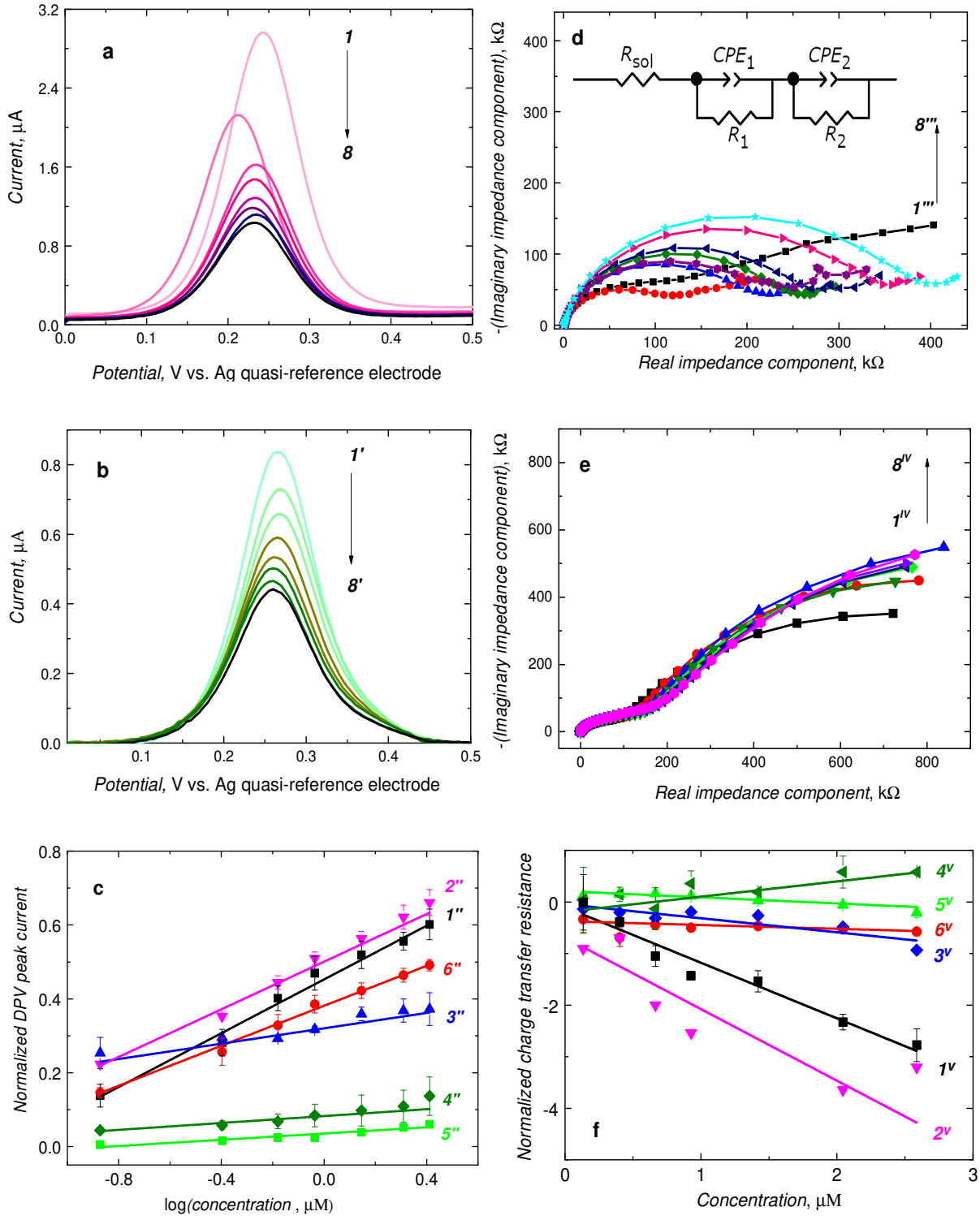

Figure 4. (a, b, and c) DPV and (d, e, and f) EIS at 0.2 V vs. Ag quasi-reference electrode curves, recorded at 2-mm diameter Au disk electrodes, coated with the polytyramine films containing (a and d) cilostazol-extracted nanoMIPs and (b and e) nanoNIPs for (*1, 1', 1'''*, and 1^{IV}) 0 nM (*2, 2', 2'''*, and 2^{IV}) 134 nM, (*3, 3', 3'''*, and 3^{IV}) 402 nM, (*4, 4', 4'''*, and 4^{IV}) 664 nM, (*5, 5',5'''*, and 5^{IV}) 927 nM, (*6, 6', 6'''*, and 6^{IV}) 1.42 µM, (*7, 7', 7'''*, and 7^{IV}) 2.04 µM, and (*8, 8',* and *8''', and* 8^{IV}) 2.58 µM cilostazol (**CIL**) in 10 mM ferrocene and 0.1 M (TBA)ClO_4 in acetonitrile. Calibration plots of (c) DPV normalized peak currents and (f) EIS determined normalized charge transfer resistance, constructed using electrodes coated

with the polytyramine film containing (*1″* - *5″*, and 1^{V} - 5^{V}) **CIL**-extracted nanoMIPs and (*6″* and 6^{V}) nanoNIPs for (*1″, 6″*, and 1^{V}, 6^{V}) **CIL**, (*2″* and 2^{V}) 3,4-dehydrocilostazol (**dhCIL)**, (*3″* and 3^{V}) **dehydroaripiprazole**, (*4″* and 4^{V}) **cholesterol**, and (5" and 5^{V}) **glucose**. Inset in (d) is the scheme of the equivalent circuit used for curve fitting where R_{sol}, R_1, and R_2 is the solution, charge transfer, and polymer film resistance, respectively.

3.6 Determining isotherm parameters of polytyramine-(nanoMIP-A) binding of cilostazol

Efforts were extended to determine the parameters of **CIL** binding by cilostazol-extracted nanoMIPs embedded in the polytyramine film. Typically, the Langmuir, Freundlich, and Langmuir-Freundlich isotherms (Rampey et al., 2004; Umpleby et al., 2004, 2001) most accurately describe this binding (Section S10 in Supplementary data). Therefore, herein, these three isotherms were tested to describe the ferrocene normalized DPV peak current dependence on the **CIL** concentration in the ferrocene solution alone (Figure S9a in Supplementary data) and the human plasma (Figure S9b in Supplementary data). Generally, the Langmuir-Freundlich isotherm best fits the experimental data of **CIL** sorption on nanoMIPs (Table 2 and Tables S1 and S2 in Supplementary data), indicating that the imprinted cavities were relatively homogeneously distributed in the polytyramine matrix, and the **CIL** analyte was chemisorbed in these cavities. Moreover, the cavities homogeneity was high (Table 2). Interestingly, the homogeneity factor was substantially higher for nanoMIPs (1.10) than for nanoNIPs (0.80). Expectedly, this difference in factors indicates that **CIL** binding in nanoNIPs encompasses a broader range of non-equivalent binding sites.

Table 2. Isotherm parameters for the nanoMIP chemosensor fitted to the normalized DPV peak current vs. **CIL** concentration in human plasma depicted in curves *1″*, *2″*, and *3″* in Figure S9b in Supplementary data.

Isotherm type	Isotherm equation	Isotherm fitting parameters			R^2
		$\Delta I_{\text{normalized DPV,max}}$	K, μM^{-1}	n	
Langmuir	$\Delta I_{\text{normalized DPV}} = \Delta I_{\text{normalized DPV,max}} \frac{K_L c_{\text{cilostazol}}}{1 + K c_{\text{cilostazol}}}$	0.92 (±0.03)	2.94 (±0.48)[a]	-	0.959
Freundlich	$\Delta I_{\text{normalized DPV}} = K_F c_{\text{cilostazol}}^{\frac{1}{n}}$	-	0.66 (±0.02)[b]	4.03 (±0.77)[d]	0.86

Langmuir-Freundlich	$\Delta I_{\text{normalized DPV}} = \Delta I_{\text{normalized DPV,max}} \frac{(K_{\text{LF}} c_{\text{cilostazol}})^n}{1 + (K_{\text{LF}} c_{\text{cilostazol}})^n}$	0.91 (±0.07)	2.96 (±0.58)[c]	1.02 (±0.25)[e]	0.949

$\Delta I_{\text{normalized DPV,max}}$ – maximum value of normalized DPV peak current
[a] K_{L} – the Langmuir constant
[b] K_{F} – the Freundlich constant
[c] K_{LF} – the Langmuir-Freundlich constant
[d] Sorption intensity
[e] Homogeneity factor

*3.7 Polytyramine-(nanoMIP-A) chemosensor selectivity to **dhCIL** metabolite and common interferences*

The nanoMIP-A molecular cavity's selectivity to metabolite **dhCIL** and common interferences in acetonitrile was estimated (Section S11 in Supplementary data) as the ratios of the slopes of the calibration plot for **CIL** to that of **dhCIL** or that of the interference. Notably, the selectivity to **dhCIL** (Table S3) was low (curves *1″* and *2″* in Figure 4c, and curves 1^{V} and 2^{V} in Figure 4f). Thus, advantageously, the chemosensor is suitable for determining analyte **CIL** and its metabolite **dhCIL** together. Figures S11 and S12 in Supplementary data show DPV peaks and EIS spectra, respectively, for cilostazol-extracted nanoMIPs immobilized in the polytyramine film-coated electrodes, for the absence and presence of **dhCIL** and interferences in a solution. The selectivity to cholesterol (curves *1″* and *4″* in Figure 4c, and curves 1^{V} and 4^{V} Figure 4f) and glucose (curves *1″* and *5″* in Figure 4c, and curves 1^{V} and 5^{V} in Figure 4f) was relatively high (Table S3) whereas to dehydroaripiprazole (curves *1″* and *3″* in Figure 4c, and curves 1^{V} and 3^{V} in Figure 4f) it was moderate (Table S3).

Next, the interactions of **CIL** and **dhCIL** analytes, and interferences, with the nanoMIP-A cavity were compared theoretically to enlighten the properties of the prepared chemosensor (Section S12 in Supplementary data). To sum up, interferences molecules (Figure S10 in Supplementary data) are located in the nanoMIP-A cavity in a way different from that of the **CIL** molecule (Figure S13 in Supplementary data) because of being too large or too small. Therefore, their interactions with the cavity are much weaker than those of **CIL** molecules. Hence, the presence of the interferences would not disturb **CIL** and **dhCIL** determination together.

*3.8 Polytyramine-(nanoMIP-A) chemosensor efficiency of **CIL** determination in real samples*

It is crucial for chemosensors clinical application to determine their performance in body fluids, such as human plasma, to estimate the matrix's effect. Toward that, gold electrodes coated with polytyramine films embedding **CIL**-extracted nanoMIP-A were herein employed to determine **CIL** in a plasma sample. Accordingly, a plasma sample (with citrate as the anticoagulant) was ten times diluted with the acetonitrile solution of 10 mM ferrocene. That resulted in the precipitation of proteins, which were then centrifuged off (Section S13 in Supplementary data). Then, samples of this solution were spiked with solutions of different concentrations of **CIL**. The UV-vis spectra recorded for the supernatant solutions to estimate possible **CIL** interaction with the plasma proteins (Figure S14 in Supplementary data) showed only a negligible **CIL** binding to the proteins (Section S14 in Supplementary data).

Notably, the chemosensor appeared successful in determining **CIL** in diluted human plasma samples (curve *1* in Figure S15a and curve *1′* in Figure S15b in Supplementary data). Moreover, the slope of 0.39 (±0.04) [1/log μM] for the calibration plot constructed only slightly deviated from that of 0.33 (±0.02) [1/log μM] in the acetonitrile-water mixture (9: 1, *v*/*v*) (curve *2* in Figure S15a and curve *2′* in Figure S15b in Supplementary data).

Recovery was calculated and has been added in Table S5 in Supplementary data.

4. Summary and conclusions

The DPV and EIS chemosensors for **CIL** and its pharmacologically active primary metabolite, **dhCIL**, determination, aided by molecular imprinting in polymers, were devised, fabricated, and compared. Four different molecularly imprinted with **CIL** polymer nanoparticles (nanoMIPs) were synthesized and examined at various functional monomers combinations. The **CIL** binding capacity was the highest if methacrylic acid was exclusively used as the functional monomer. The resulting nanoMIP-A particles were then successfully embedded by sedimentation, followed by tyramine electropolymerization, in a polytyramine film deposited on an Au electrode surface. Both DPV and EIS chemosensors appeared suitable for determining **CIL** and **dhCIL** with the LOD of 93.5 (±2.2) and 86.5 (±4.6) nM **CIL**, respectively, in the linear dynamic concentration range of 0.135 to 2.58 μM, and appreciably high selectivity to common interferences including cholesterol, glucose, and moderate to dehydroaripiprazole. Remarkably, such relatively low LOD values for the **CIL** drug substance have not yet been reported for any electrochemical method (Table S4 in Supplementary data).

Computer simulations permitted analyzing the interactions governed by the analytes' sorption at the molecular level. Generally, the Langmuir-Freundlich isotherm best fits the experimental data of **CIL** sorption on nanoMIPs, indicating that the imprinted cavities were relatively homogeneously distributed in the MIP matrix with the **CIL** molecules chemisorbed in these cavities.

5. Future prospective

We have demonstrated that the chemosensors fabricated may help diagnostics within the **CIL** and **dhCIL** concentration ranges in body fluids required in the future clinical trials of cilostazol. Our future research will aim to make the chemosensor reusable and cross-validate its performance with LC-MS, GC-MS, etc.

CRediT authorship contribution statement

Jyoti: Investigation, Conceptualization, Validation, Writing - original draft. **Carlo Gonzato:** Supervision. **Franck Merlier:** Investigation. **Teresa Żołek:** Methodology, Formal analysis, Writing an original draft. **Dorota Maciejewska:** Formal analysis, Writing - review & editing. **Krzysztof Noworyta:** Formal analysis, Data curation, Funding acquisition, Supervision. **Andrzej Kutner:** Writing - review & editing. **Piyush Sindhu Sharma:** Conceptualization, Supervision. **Karsten Haupt:** Supervision, Writing - review & editing. **Wlodzimierz Kutner:** Supervision, Writing - review & editing.

Declaration of competing interest

The authors declare that they have no known competing financial interests or personal relationships that could have influenced the work reported in this paper**.**

Acknowledgments

The Polish National Science Foundation (NCN) financially supported the present research through Grant No. 2015/19/B/ST4/03743 to KN. The Erasmus Plus Program of the EU and the Mobility grant of the IPC PAS supported the Jyoti secondment to the Université de Technologie de Compiègne.

References

Ahmad, O.S., Bedwell, T.S., Esen, C., Garcia-Cruz, A., Piletsky, S.A., 2019. Trends Biotechnol. 37, 294–309.

Akiyama, H., Kudo, S., Shimizu, T., 1985. Arzneimittelforschung. 35, 1124—1132.

Alexander, C., Andersson, H.S., Andersson, L.I., Ansell, R.J., Kirsch, N., Nicholls, I.A., O'Mahony, J., Whitcombe, M.J., 2006. J. Mol. Recognit. 19, 106–180.

Attia, M.S., Mahmoud, W.H., Youssef, A.O., Mostafa, M.S., 2011. J. Fluoresc. 21, 2229–2235.

Azizi, A., Bottaro, C.S., 2020. J. Chromatogr. A. 1614, 460603.

Bedwell, T.S., Whitcombe, M.J., 2016. Anal. Bioanal. Chem. 408, 1735–1751.

Belbruno, J.J., 2019. Chem. Rev. 119, 94–119.

Bhatt, N.M., Chavada, V.D., Patel, D.P., Sharma, P., Sanyal, M., Shrivastav, P.S., 2015. J. Pharm. Anal. 5, 1–11.

Bramer, S.L., Forbes, W.P., Mallikaarjun, S., 1999. Clin. Pharmacokinet. 37, 1–11.

Bramer, S.L., Tata, P.N. V., Vengurlekar, S.S., Brisson, J.H., 2001. J. Pharm. Biomed. Anal. 26, 637–650.

Chaitidou, S., Kotrotsiou, O., Kotti, K., Kammona, O., Bukhari, M., Kiparissides, C., 2008. Mater. Sci. Eng. B Solid-State Mater. Adv. Technol. 152, 55–59.

Chen, L., Wang, X., Lu, W., Wu, X., Li, J., 2016. Chem. Soc. Rev. 45, 2137–2211.

Cummins, W., Duggan, P., McLoughlin, P., 2006. Biosens. Bioelectron. 22, 372–380.

Dong, C., Shi, H., Han, Y., Yang, Y., Wang, R., Men, J., 2021. Eur. Polym. J. 145, 110231.

Douglas, J.S., Holmes, D.R., Kereiakes, D.J., Grines, C.L., Block, E., Ghazzal, Z.M.B., Morris, D.C., Liberman, H., Parker, K., Jurkovitz, C., Murrah, N., Foster, J., Hyde, P., Mancini, G.B.J., Weintraub, W.S., 2005. Circulation 112, 2826–2832.

El-Akaad, S., Mohamed, M.A., Abdelwahab, N.S., Abdelaleem, E.A., De Saeger, S., Beloglazova, N., 2020. Sci. Rep. 10, 1–10.

El-Schich, Z., Zhang, Y., Feith, M., Beyer, S., Sternbæk, L., Ohlsson, L., Stollenwerk, M., Wingren, A.G., 2020. Biotechniques 69, 407–420.

Ezoji, H., Rahimnejad, M., 2019. Nanoparticles-based Electrochemical Sensors and Biosensors. In: Luque, R., Prinsen, P. (Eds.), Nanoparticle Design and Characterization for Catalytic Applications in Sustainable Chemistry. The Royal Society of Chemistry, Cambridge, pp. 329–345.

Fuchs, Y., Linares, A. V., Mayes, A.G., Haupt, K., Soppera, O., 2011. Chem. Mater. 23, 3645–3651.

Goud, K.Y., Reddy, K.K., Khorshed, A., Kumar, V.S., Mishra, R.K., Oraby, M., Ibrahim, A.H., Kim, H., Gobi, K.V., 2021. Biosens. Bioelectron. 180, 113112.

Haupt, K., Dzgoev, A., Mosbach, K., 1998. Anal. Chem. 70, 628–631.

Haupt, K., Mosbach, K., 2000. Chem. Rev. 100, 2495–2504.

Haupt, K., Rangel, P.X.M., Tse, B.B.S., 2020. Chem. Rev. 120, 9554–9582.

Hiramatsu, M., Takiguchi, O., Nishiyama, A., 2010. Br. J. Pharmacol. 161, 1899–1912.

Hishikawa, N., Fukui, Y., Sato, K., Ohta, Y., Yamashita, T., Abe, K., 2017. Geriatr. Gerontol. Int. 17, 1384–1391.

Ibrahim, F., El-din, M.S., El-aziz, H.A., 2016. Br. J. Pharm. Res. 12, 1–15.

Ikeda, Y., Sudo, T., Kimura, Y., 2013. Cilostazol. in: Alan D. Michelson (Ed.), Cilostazol, in Platelets. Massachusetts, USA, pp. 1171–1183.

Jain, R., Sharma, R., 2012. J. Appl. Electrochem. 42, 341–348.

Karlsson, J.G., Karlsson, B., Andersson, L.I., Nicholls, I.A., 2004. Analyst 129, 456–462.

Lee, S.W., Park, S.W., Kim, Y.H., Yun, S.C., Park, D.W., Lee, C.W., Hong, M.K., Kim, H.S., Ko, J.K., Park, J.H., Lee, J.H., Choi, S.W., Seong, I.W., Cho, Y.H., Lee, N.H., Kim, J.H., Chun, K.J., Park, S.J., 2008. J. Am. Coll. Cardiol. 51, 1181–1187.

Mijangos, I., Navarro-Villoslada, F., Guerreiro, A., Piletska, E., Chianella, I., Karim, K., Turner, A., Piletsky, S., 2006. Biosens. Bioelectron. 22, 381–387.

Ndunda, E.N., Mizaikoff, B., 2016. Analyst 141, 3141–3156.

NIH U.S. National Library of Medicine, ClinicalTrials.gov., https://clinicaltrials.gov/ct2/results?recrs=&cond=combined+treatment&term=cilostazol&cntry=&state=&city=&dist=, as accessed on 6.6.21

Nirogi, R.V.S., Kandikere, V.N., Shukla, M., Mudigonda, K., Shrivasthava, W., Datla, P. V., Yerramilli, A., 2006. Anal. Bioanal. Chem. 384, 780–790.

O'Shannessy, D.J., Ekberg, B., Mosbach, K., 1989. Anal. Biochem. 177, 144–149.

Pareek, D., Jain, S., Basniwal, P., Jain, D., 2014. Acta Chromatogr. 26, 283–296.

Park, S.H., Kim, J.H., Bae, S.S., Hong, K.W., Lee, D.S., Leem, J.Y., Choi, B.T., Shin, H.K., 2011. Biochem. Biophys. Res. Commun. 408, 602–608.

Pérez-Moral, N., Mayes, A.G., 2004. Langmuir 20, 3775–3779.

Poma, A., Guerreiro, A., Whitcombe, M.J., Elena, V., 2013. Adv Funct Mater. 23, 2821–2827.

Puoci, F., Cirillo, G., Curcio, M., Parisi, O.I., Iemma, F., Picci, N., 2011. Expert Opin. Drug Deliv. 8, 1379–1393.

Ramanavicius, S., Jagminas, A., Ramanavicius, A., 2021. Polymers (Basel). 13, 974.

Ramanavicius, S., Ramanavicius, A., 2021. Polymers (Basel). 13, 1–19.

Rampey, A.M., Umpleby, R.J., Rushton, G.T., Iseman, J.C., Shah, R.N., Shimizu, K.D., 2004. Anal. Chem. 76, 1123–1133.

Rutkowska, M., Płotka-Wasylka, J., Morrison, C., Wieczorek, P.P., Namieśnik, J., Marć, M., 2018. TrAC - Trends Anal. Chem. 102, 91–102.

Saito, S., Ihara, M., 2014. Front. Aging Neurosci. 6, 1–11.

Saitoh, S., Saito, T., Otake, A., Owada, T., Mitsugi, M., Hashimoto, H., Maruyama, Y., 1993. Arterioscler. Thromb. Vasc. Biol. 13, 563–570.

Sakurai, H., Hanyu, H., Sato, T., Kume, K., Hirao, K., Kanetaka, H., Iwamoto, T., 2013. Geriatr. Gerontol. Int. 13, 90–97.

Sharma, P.S., Garcia-Cruz, A., Cieplak, M., Noworyta, K.R., Kutner, W., 2019. Curr. Opin. Electrochem. 16, 50–56.

Sharma, P.S., Iskierko, Z., Noworyta, K., Cieplak, M., Borowicz, P., Lisowski, W., D'Souza, F., Kutner, W., 2018. Biosens. Bioelectron. 100, 251–258.

Taguchi, A., Takata, Y., Ihara, M., Kasahara, Y., Tsuji, M., Nishino, M., Stern, D., Okada,

M., 2013. Psychogeriatrics 13, 164–169.

Tonelli, D., Scavetta, E., Gualandi, I., 2019. Sensors (Switzerland) 19, 1186.

Umpleby, R.J., Baxter, S.C., Chen, Y., Shah, R.N., Shimizu, K.D., 2001. Anal. Chem. 73, 4584–4591.

Umpleby, R.J., Baxter, S.C., Rampey, A.M., Rushton, G.T., Chen, Y., Shimizu, K.D., 2004. J. Chromatogr. B 804, 141–149.

Vaughan, A.D., Sizemore, S.P., Byrne, M.E., 2007. Polymer (Guildf). 48, 74–81.

Vlatakis, G., Andersson, L.I., Müller, R., Mosbach, K., 1993. Nature 361, 645–647.

Wulff, G., 2002. Chem. Rev. 102, 1–28.

Xie, X., Bu, Y., Wang, S., 2016. Rev. Anal. Chem. 35, 87–97.

Yang, H.H., Zhang, S.Q., Tan, F., Zhuang, Z.X., Wang, X.R., 2005. J. Am. Chem. Soc. 127, 1378–1379.

Yarman, A., Kurbanoglu, S., Zebger, I., Scheller, F.W., 2021. Sens. Actuators, B 330, 129369.

Ye, L., A. G. Cormack, P., Mosbach, K., 1999. Anal. Commun. 36, 35–38.

Yeon, K.J., Park, Y.J., Park, K.M., Park, J.S., Kim, M.K., Kim, Y.B., Kim, C.K., Jeong, K., Park, Y.J., Park, K.M., Park, J.S., Park, J., 2005. J. Liq. Chromatogr. Relat. Technol. 28, 109–120.

Yilmaz, E., Mosbach, K., Haupt, K., 1999. Anal. Commun. 36, 167–170.

Yoshimi, Y., Ohdaira, R., Iiyama, C., Sakai, K., 2001. Sens. Actuators, B 73, 49–53.

Zhao, J., Harada, N., Kurihara, H., Nakagata, N., Okajima, K., 2010. Neuropharmacology 58, 774–783.

Zhao, W., Zhang, R., Xu, S., Cai, J., Zhu, X., Zhu, Y., Wei, W., Liu, X., 2018. Biosens. Bioelectron. 100, 497–503.